

Tunable Inter-Edge Interactions in a Bilayer Graphene Quantum Hall Antidot

Mario Di Luca,¹ Emily Hajigeorgiou,¹ Zekang Zhou,¹ Tengyan Feng,¹ Kenji Watanabe,² Takashi Taniguchi,³ Ferdinand Kuemmeth,⁴ and Mitali Banerjee^{1,5,*}

¹*Institute of Physics, École Polytechnique Fédérale de Lausanne (EPFL), CH-1015 Lausanne, Switzerland*

²*Research Center for Functional Materials, National Institute for Materials Science, 1-1 Namiki, Tsukuba 305-0044, Japan*

³*International Center for Materials Nanoarchitectonics,*

National Institute for Materials Science, 1-1 Namiki, Tsukuba 305-0044, Japan

⁴*Institute of Experimental and Applied Physics, University of Regensburg, Regensburg D-93053, Germany*

⁵*Center for Quantum Science and Engineering (QSE Center),*

École Polytechnique Fédérale de Lausanne (EPFL), CH-1015 Lausanne, Switzerland

Electronic interferometers in the quantum Hall regime are one of the best tools to study the statistical properties of localized quasiparticles in the topologically protected bulk. However, since their behavior is probed via chiral edge modes, bulk-to-edge and inter-edge interactions are two important effects that affect the observations. Moreover, almost all kinds of interferometers heavily rely on a pair of high-quality quantum point contacts where the presence of impurities significantly modifies the behavior of such constrictions, which in turn can alter the outcome of the measurements. Antidots, potential hills in the quantum Hall regime, are particularly valuable in this context, as they overcome the geometric limitations of conventional geometries and act as controlled impurities within a quantum point contact. Furthermore, antidots allow for quasiparticle charge detection through simple conductance measurements, replacing the need for complex techniques such as shot noise. Here, we use a gate-defined bilayer graphene antidot, operated in the Coulomb-dominated regime. By varying the antidot potential, we can tune inter-edge interactions, enabling a crossover from a single-dot to a double-dot behavior. In the latter, strong coupling between the two edge states leads to edge-state pairing, resulting in a measured doubling of the tunneling charge. We find that in certain regimes, the inter-edge coupling completely dominates over other energy scales of the system, overshadowing the interference effects these devices are mainly designed to probe. These results highlight the significant role of inter-edge interactions and establish antidots as a versatile platform for exploring quantum Hall interferometry.

Electronic interferometry in the quantum Hall regime utilizes chiral one-dimensional edge channels to study the statistical exchange properties of emergent particles. The most common type of electronic interferometer is the quantum dot interferometer, also known as a Fabry-Pérot interferometer (FPI) [1]. FPIs have long been used both in GaAs and graphene in the integer [2–6] and fractional quantum Hall regimes (QH) to probe electron interference and more recently to probe the exchange statistics of anyons [7–11]. However, these observations can still be influenced by bulk impurities and charging effects, which may mask the true signatures of the quasiparticles. In particular, when the interfering edge states are strongly coupled to compressible states in the bulk, this interaction can dominate the response of the system and obscure the expected Aharonov-Bohm (AB) oscillations [1]. This is why new geometries that do not suffer from bulk-to-edge coupling, such as two-path Mach-Zehnder [12–14] and chiral Mach-Zehnder [15, 16] interferometers, have been explored.

Another possible geometry that avoids bulk-to-edge coupling is the quantum Hall antidot (AD), where interference occurs around a potential hill [17–19]. Traditionally, antidots have been extensively studied in GaAs heterostructures for electron interferometry in the inte-

ger quantum Hall regime [20–23], and they have played a crucial role in the first detection of fractionally charged quasiparticles [24–26]. Antidots are predicted to be an ideal platform for studying non-Abelian states [27, 28] and to controllably braid non-Abelian quasiparticles [29]. In an antidot, the most important energy scale is the energy spacing determined by the antidot diameter and the edge mode velocity with a larger edge mode velocity leading to higher energy scales.

Graphene, a one-atom thick hexagonal layer of carbon atoms, serves as a natural 2D electron gas, and devices based on graphene are a perfect substitute platform due to its unique electronic band structure and its high intrinsic Fermi velocity [30, 31]. However, despite its simple geometry, not much has been explored in graphene due to the challenges of fabricating high-quality tunable antidots in van der Waals heterostructures. The few efforts in monolayer graphene have been limited to the study of localized edges via scanning tunneling microscopy (STM) [32–34] and lithographically etched structures in hBN-encapsulated or suspended graphene [35, 36]. However, both of these approaches lack the tunability to control the coupling between the extended edges and the antidot bound states.

Here, we present a dual gate-defined bilayer graphene antidot, where the antidot is fully electrostatically defined and controlled, enabling tunability beyond previous designs and allowing the study of transitions across

* mitali.banerjee@epfl.ch

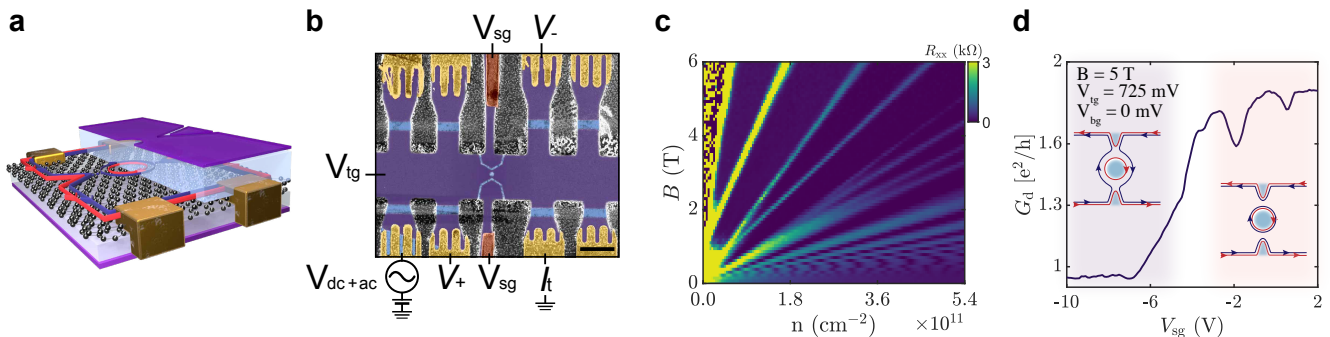


FIG. 1: Gate-defined antidot in bilayer graphene. **a**, Schematic of the device at $\nu = 2$ showing oscillations of the inner edge state (blue), while the outer edge state (red) is fully transmitted. The graphite gates are shown in purple and the hBN in blue. Only half of the top hBN and top graphite gate is shown for clarity. **b**, False-color scanning electron microscope image of an antidot device. The ohmic contacts are shown in gold, the palladium contacts to the graphite top gate in dark orange, the graphite in purple, and in blue the top hBN is visible in places where the top graphite has been etched. The antidot area is defined by the etched circle in the top graphite. A voltage of $V_{ac} = 10 \mu\text{V}$ was applied, with measurement of the transmitted (I_t) current. Voltage was measured immediately before the antidot (V_+), and after the drain (V_-). The scale bar is $2 \mu\text{m}$. **c**, Longitudinal resistance R_{xx} fan diagram measured outside the antidot as a function of the carrier density n . **d**, Transmitted conductance for $\nu = 2$ as a function of the side gates V_{sg} . Each inset schematically represents the system at the corresponding voltage range.

different interaction regimes. The antidot is mainly operated in the Coulomb interaction dominated regime as a way to study inter-edge coupling in the integer quantum Hall regime. By varying the antidot potential, we control inter-edge interactions, transitioning between *weakly* to *strongly coupled* regimes. In the *weakly coupled* regime, we demonstrate Coulomb-dominated oscillations at integer filling factors ν with a magnetic field period corresponding to a flux of ϕ_0/ν and a gate voltage period corresponding to the electron tunneling charge. In the *strongly coupled* regime, we show the appearance of different oscillations in even integer filling factors. These oscillations are interpreted as a coupling between the two innermost edge states, similar to the report of STM measurements in monolayer graphene [34].

To study the interference in the strongly correlated fractional quantum Hall states, where multiple edges happen to interact, it is necessary to first understand the nature of inter-edge interactions in the non-interacting integer quantum Hall states. Our results highlight the versatility of antidots in the quantum Hall regime and their potential to study quasiparticle interactions in fractional quantum Hall systems.

DEVICE DESCRIPTION

An antidot is a potential hill introduced into a two-dimensional electron gas in a perpendicular magnetic field. In the quantum Hall regime, chiral edge modes encircle the antidot while extended channels carry current

along the device boundaries. The main effect of the antidot potential is to lift the degeneracy of the Landau levels (LL) encircling it, by splitting the energy spectrum into quantized levels, where each can host one charge carrier [33, 34]. The energy splitting is related to the velocity of the edge mode v and the diameter of the antidot D_{AD} , $\delta\epsilon \sim \hbar v/D_{AD}$. By tuning an external parameter, such as the magnetic field or the top and bottom gate voltages, it is possible to control the number of electrons confined in the antidot-bound states and to detect them through resonant tunneling between the extended edge channels and the quantized antidot-bound states.

In figure 1-a, we present a gate-defined bilayer graphene (BLG) antidot device. The antidot is electrostatically defined by an etched hole in the top graphite, with its density tuned near the highly resistive $\nu = 0$ state via a negative voltage applied to the bottom graphite gate (BG). The BLG layer is encapsulated between two layers of hexagonal boron nitride (hBN), as shown in the schematic in figure 1-a. The device is fabricated using a standard van der Waals dry pick-up technique, described in the Methods section. The charge carrier density of BLG is tuned via voltages applied to both the bottom and the top graphite. Lithographically etched line cuts in the top graphite define the top gate (TG) and two side gates (SG) as shown in figure 1-b. The TG sets the filling factor in the bulk ν_b , and by applying a negative voltage to the SG we control the number of transmitted edges through the constriction, defined as the ensemble of side gates and antidot. In the main text, we denote the bulk filling factor by the continuous variable ν_b , while ν will refer to the integer value closest to

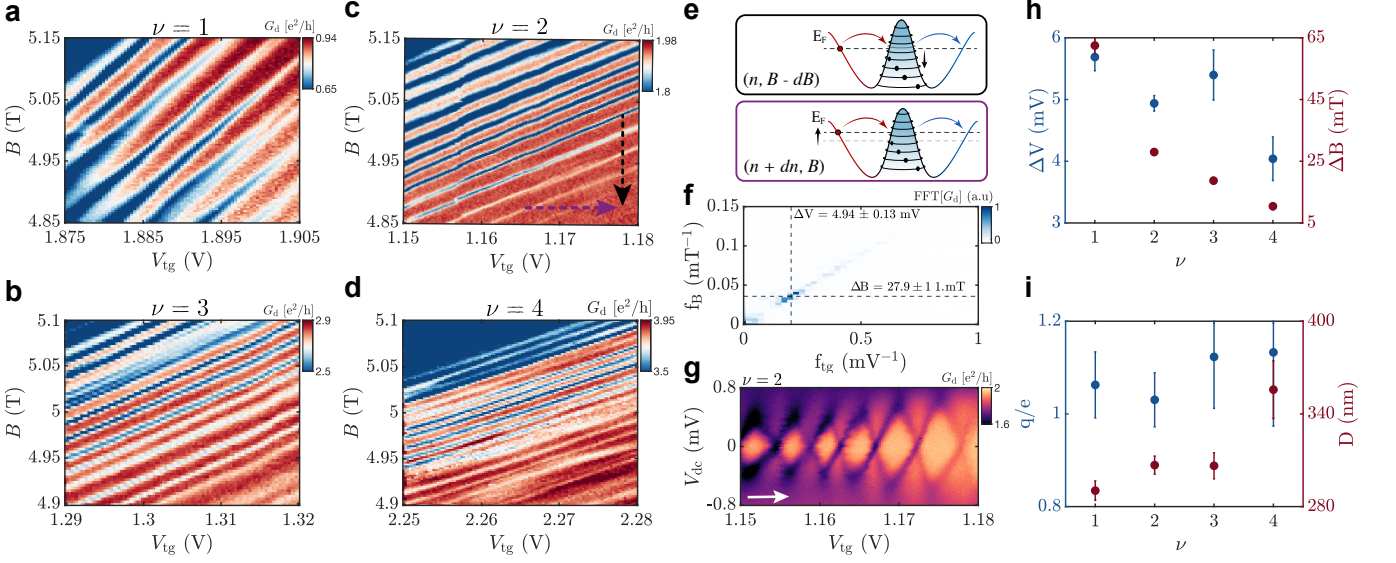


FIG. 2: Coulomb dominated oscillations for integer filling factor. **a-d**, Diagonal conductance G_d oscillations as a function of the top gate voltage (V_{tg}) and the magnetic field (B) for inner-edge filling factors $\nu = 1 - 4$. **e**, Schematic of the oscillations mechanism when varying the magnetic field (top panel) or the charge carrier density (bottom panel), corresponding respectively to the black and purple arrow in panel **c**. **f**, 2D Fast Fourier transform (FFT) of the oscillations for $\nu = 2$. **g**, Diagonal conductance G_d as a function of top gate voltage and DC bias displaying characteristic Coulomb diamonds for $\nu = 2$ at $B = 5$ T. The white arrow in panel **g** indicates an increasing number of electrons bound to the antidot. **h**, Top gate period ΔV (blue) and magnetic field period ΔB (red) as a function of the filling factor ν . **i**, Tunneling charge (blue) and oscillating antidot diameter (red) as a function of the filling factor ν .

ν_b .

The device has ohmic contacts along both upstream and downstream extended edges, allowing for current injection and differential chemical potential measurements across the antidot. Unless otherwise stated, all measurements were performed with an applied voltage of $V_{ac} = 10 \mu\text{V}$, while measuring the transmitted current, I_t . Furthermore, longitudinal resistance R_{xx} is measured before the antidot (not reported in the schematic in figure 1-b), and measurement of the voltage drop ($V_+ - V_-$) gives the diagonal conductance through the antidot, $G_d = I_t / (V_+ - V_-) \equiv \nu_c e^2 / h$, where ν_c is the filling factor of the constriction.

To maintain ballistic edge states encircling the antidot, its diameter must be significantly larger than the magnetic length (l_B), $D_{AD} \gg l_B \approx \frac{24 \text{ nm}}{\sqrt{B[\text{T}]}}$. In our device, atomic force microscopy measurements show a lithographic diameter of the graphite antidot of $D_{AD} = 200 \pm 5 \text{ nm}$. However, because of the electric field propagation through the top thicker hBN layer, the effective area of the antidot at the graphene surface is expected to be larger. From COMSOL simulations, using a top hBN thickness of approximately 56 nm, we estimate the effective antidot diameter to be around $\sim 300 \text{ nm}$ (see Supplementary Materials).

The device is initially characterized by studying the development of Landau levels as a function of electron density and magnetic field, as shown in figure 1-c. In BLG Landau levels exhibit a fourfold degeneracy due to spin and valley degrees of freedom. Additionally, the two lowest orbital levels share the same energy due to the LL energy dispersion, given by $E = \hbar\omega_c \sqrt{N(N-1)}$ where ω_c is the frequency of the cyclotron orbit. As the magnetic field increases, the Landau level degeneracy is lifted first for the valley, followed by spin splitting, and finally by orbital number splitting [37, 38]. Figure 1-c shows the dependence of BLG Landau levels on the carrier density and the magnetic field.

COULOMB OSCILLATIONS AT INTEGER FILLING FACTORS

We begin by studying the device at a perpendicular magnetic field of $B = 5 \text{ T}$ at integer bulk filling factors, $\nu = 1 - 4$. By tuning the SG voltages, the innermost edge states can be brought into proximity with the antidot-bound states. Figure 1-d shows the diagonal conductance G_d as a function of the side gates voltage V_{sg} at $\nu = 2$. As V_{sg} decreases, the inner edge can be selectively partitioned, crossing over from the full trans-

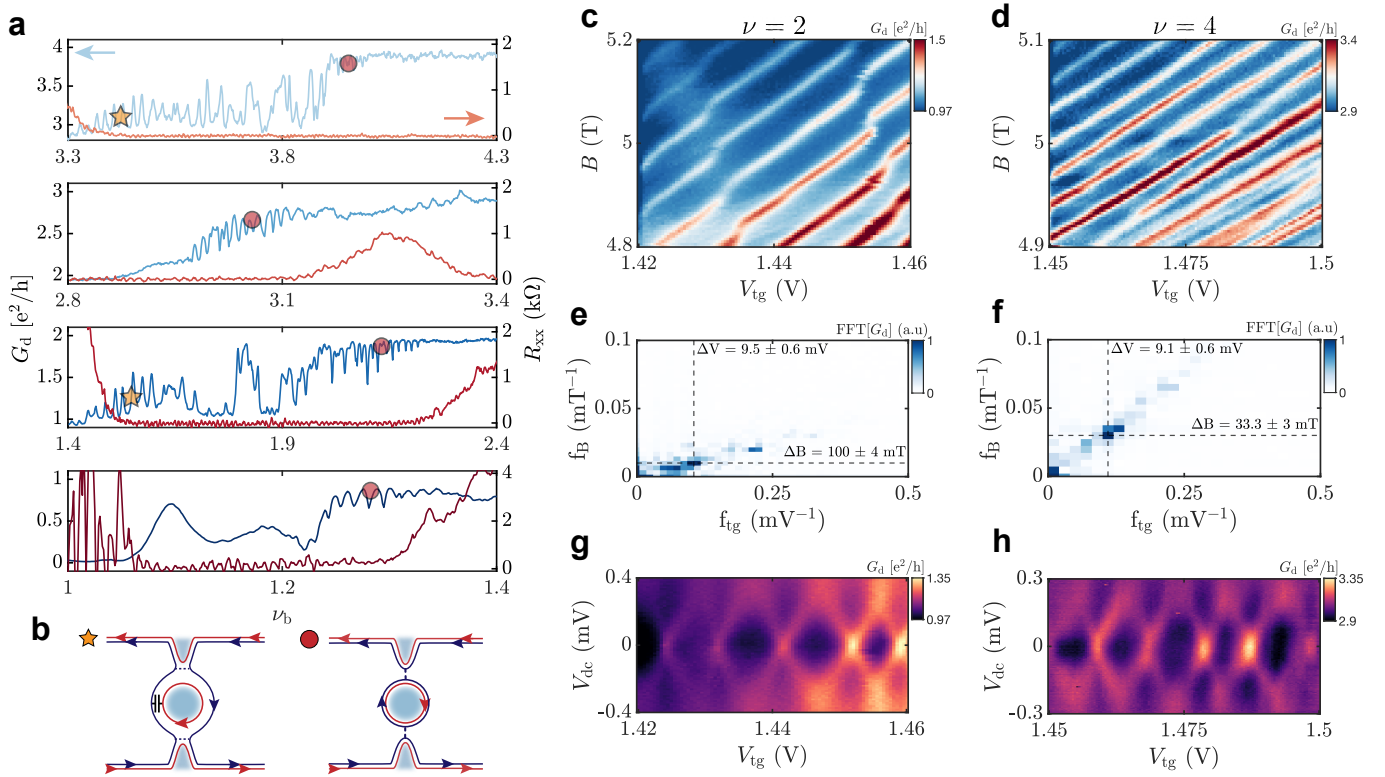


FIG. 3: Inter-Edge coupling in even filling factors **a**, Diagonal conductance (blue) and longitudinal resistance (in red) as a function of the bulk filling factor ν_b . Red dots mark regions of oscillations reported in figure 2. Yellow stars mark the appearance of the strongly interacting oscillations. **b**, Schematic of the interaction for the two innermost edges in both regimes. In the red dot schematic, the antidot is weakly coupled to the extended edge. For the yellow star, it is *strongly coupled* and the two innermost edges are capacitively coupled. In both cases, it is the inner edge that interferes. The oscillations at both filling factors display phase slips, characterized by a lower oscillation amplitude, typical of Coulomb coupling between two edge modes. **c-d**, Diagonal conductance oscillation at $\nu = 2$ and $\nu = 4$ in the *strongly coupled* regime corresponding to the yellow star. **e-f**, 2D-FFT showing a larger period than the non-interacting one. **g-h**, Diagonal conductance G_d as a function of top gate voltage and DC bias still displaying the Coulomb Diamonds.

mission ($V_{sg} \approx 2$ V) to full reflection ($V_{sg} \approx -8$ V). In this device, the diagonal conductance is 10% lower than the expected quantized value due to a non-zero initial reflection of the constriction.

When the constriction is set on a QH plateau, charge transport between the counter-propagating edges is suppressed, resulting in constant G_d . However, when the inner extended edge is brought into proximity to the antidot-bound states, $\nu_b > \nu_c > 1$, charge carriers can tunnel from the extended edges to the antidot. When the chemical potential of an antidot-bound state aligns with the Fermi level, an electron can tunnel resonantly through the antidot, leading to a dip in the tunneling conductance G_d . As the magnetic field is adiabatically varied by a small amount (by a fraction of the quantum flux), the antidot-bound states adjust to maintain a constant enclosed flux. As the edge states move over the antidot potential to adjust their size, their energy changes

accordingly. This process generates periodic oscillations in G_d with a magnetic field period of $\Delta B = \frac{\phi_0}{\nu_{int} A}$, where ϕ_0 is the quantum of magnetic flux, ν_{int} is the filling factor of the interfering edge and $A = \pi D_{AD}^2/4$ is the antidot area [39].

The oscillations can also be controlled electrostatically using the TG and BG. By sweeping both gate voltages simultaneously, while maintaining a constant electron density n , the antidot area can be changed. The oscillations observed using this method are provided in the supplementary materials.

Another method involves varying the electron density around the antidot, allowing for tunneling at periodic voltage values of the density-controlling gate. This method has the advantage of allowing the measurement of the tunneling charge, $\Delta V = \frac{q}{CA}$, where C is the capacitance per unit area of the swept gate, q the tunneling charge and ΔV the gate period [24, 35]. In our device,

the density can be tuned either by adjusting the TG or BG voltage, while keeping the other gates constant. In the following sections, we vary the electron density using only the TG, with the BG fixed (for oscillations using the BG see the supplementary materials).

For each filling factor, the SG voltages are set such that the transmission is $t \simeq 1$, a regime we refer to as *weakly coupled* regime, because the antidot is nearly isolated from the extended edge state. Figure 2-a-d shows oscillations in the diagonal conductance as a function of the TG voltage, V_{tg} , and the magnetic field for the inner edge of filling factor $\nu = 1 - 4$. A dip in the conductance appears each time carriers can transfer from the higher to the lower potential edge through the antidot-bound states, as illustrated in the schematic in figure 2-e. To determine the oscillation period, we perform a two-dimensional Fast Fourier Transform (2D-FFT), shown in figure 2-f for $\nu = 2$. The plot reveals a sharp peak corresponding to the primary oscillations. From the main peak frequency, we extract the magnetic field period ΔB and the TG period ΔV . Figure 2-h reports the periods for each filling factor. Notably, ΔV slightly decreases with increasing filling factor due to the increasing number of edge states encircling it [33]. Meanwhile, ΔB monotonically decreases, as expected from the ϕ_0/ν dependence [19, 39].

The latter can be used to compute the antidot diameter $D_{\text{AD}} = 2\sqrt{\phi_0/\pi\Delta B\nu_{\text{int}}}$ reported in figure 2-i. As previously mentioned, the measured diameter increases with the filling factor and it is in good agreement with the expected values obtained from numerical simulations at zero magnetic field. Using the geometric capacitance of the TG $C = 451 \mu\text{Fm}^{-2}$ (see suppl. materials) and substituting the area dependence from the magnetic field and gate period, the charge of the tunneling particle can be written as

$$q = \frac{C\Delta V\phi_0}{\Delta B\nu_{\text{int}}} \quad (1)$$

Figure 2-i shows the computed charge (blue) for different filling factors. The calculated charge is 5-10% higher than the expected value of one electron per period. We attribute this discrepancy to a dependence of the antidot potential on the TG voltage. As the TG voltage increases so does the antidot area, causing the antidot-bound energy levels to shift upward along the potential hill to maintain constant flux. Oscillations by only changing the area at constant density (reported in the suppl. materials) show a TG periodicity of $\Delta V \simeq 33 \text{ mV}$, which is almost seven times larger than the one obtained when changing the density. This period is obtained by combining the effects of BG and TG together, so we expect the period of only TG to be larger. This suggests that the energy levels of the antidot-bound states shift up by at least one level every seven electron jumps, which is consistent with a 10% overestimation of the electron charge. To confirm this theory, we performed oscillations using

only BG (see supp. materials) that show an estimate of the tunneling charge of about 5% less than the electron charge.

Finally, we study the DC bias V_{dc} dependence of the oscillations. Figure 2-g shows the diagonal conductance oscillations as a function of the TG voltage and the dc bias for the inner mode of $\nu = 2$. G_{d} exhibits a Coulomb diamond behavior, characterized by trapezoidal regions where tunneling through the antidot is suppressed. For $\nu = 2$, we observe that the excitation energy increases as the TG voltage increases. This is likely due to a change of the antidot potential slope, which results in a higher charge carrier velocity and thus a larger energy gap. For each filling factor, we extract a charging energy, which is on the order of $300 - 600 \mu\text{eV}$ and depends on the energy level spacing. To estimate the energy level spacing without considering electron-electron interactions, we can use the expression $\delta\epsilon = 2\hbar v/D_{\text{AD}}$ with \hbar is the reduced Planck's constant and $v = -\frac{1}{eB} \frac{\partial V}{\partial r}$ is the drift velocity of the charge carriers on the antidot potential V . In graphene interferometers, a typical drift velocity is $v = 10^5 \text{ m/s}$ [4, 5, 9, 11, 40, 41]. Assuming an antidot diameter D_{AD} of 300 nm, the energy gap is $\delta\epsilon \simeq 450 \mu\text{eV}$. This estimated energy gap aligns well with experimental observations without the need for electron-electron interactions.

For the 2D-FFT and the source-drain bias measurements of the other filling factors, see the supplementary materials.

INTER-EDGE COUPLING

Next, we study the inter-edge interactions by varying the antidot potential and its coupling to the extended edges. In the previously examined case, the constriction filling factor is close to the bulk filling factor ($\nu_c \simeq \nu_b$), tunneling between the antidot and the extended edge was weak, and the oscillations followed the single level tunneling as reported in earlier experiments in GaAs and suspended monolayer graphene antidots [18, 35, 39]. In addition, as the antidot potential decreases, the energy spacing between two consecutive antidot-bound states also decreases, making it easier for them to couple. Figure 3-a shows the diagonal conductance across the antidot (shades of blue) and the longitudinal resistance R_{xx} measured outside the antidot (shades of red) for different bulk filling factors. The regions where oscillations were observed in the previous section are marked with red dots.

As ν_b decreases while remaining on the same plateau ($R_{\text{xx}} = 0 \Omega$), we observe the emergence of new oscillations with a larger period for even filling factors at the edge of the resistance plateau (marked with a yellow star in figure 3-a). The schematic representation of these different oscillation patterns is shown in figure 3-b, where only the two innermost edges are illustrated for both regimes. These oscillations appear only in even

filling factors ($\nu = 2, 4$), whereas for odd filling factors ($\nu = 1, 3$) only the smaller period oscillations are observed (Figure 2). Figure 3-**c,d** shows the oscillations at $\nu = 2$ and $\nu = 4$, respectively. These oscillations exhibit a larger period than the one in the *weakly coupled* regime as shown by the 2D-FFT in figure 3-**e,f**.

We rule out the possibility of Aharonov-Bohm oscillations with a magnetic period corresponding to ϕ_0 because the extracted oscillation diameter at $\nu = 2$, $D_{AD} = 230 \pm 14$ nm, is smaller than that at $\nu = 1$ and also smaller than the value predicted by COMSOL simulations at zero magnetic field. Moreover, oscillations in the AB regime should only be caused by a change in area, or magnetic field, not by a change in density, but the slope of oscillations in figure 3-**c,d** supports oscillations caused solely by a density change. As shown in figure 2, an increase in the TG voltage corresponds to an increase in the antidot area, but this variation is negligible compared to the density change. Finally, the source-drain measurements in figure 3-**g,h** display Coulomb diamonds.

All these together let us conclude that the oscillations arise from a different mechanism other than the Aharonov-Bohm interference. The oscillations at both filling factors display phase slips typical of Coulomb coupling between the two edge modes. This feature has been previously reported in STM measurements on graphene dots [34], in quantum dots in the QH regime [42, 43] and in strongly coupled edge channels in a graphene Fabry-Pérot interferometer [40, 44] and can be explained using a double-dot description.

We suggest that these interactions arise from a coupling between the two innermost edges of even filling factors. In bilayer graphene the zeroth ($N = 0$) and first ($N = 1$) Landau levels are degenerate. Due to the orbital degeneracy, for even filling factors, two adjacent edges at low displacement field ($D < 100$ mV/nm), as it is the case in this paper, share the same valley pseudo-spin and spin but differ in their orbital index—either the $N = 0$ or $N = 1$ [37, 38, 45]. In contrast, for odd filling factors, this does not occur and the two innermost Landau levels have opposite spins, similar to what is observed in GaAs systems. As a consequence for even filling factors the two highest Landau levels are separated by a smaller energy gap, making it easier for them to interact.

To understand this behavior we use a capacitive coupling model, in which the two innermost spin- and valley-polarized edges are capacitively coupled. The system's energy can be expressed as:

$$E = \frac{1}{2}K_1\delta Q_1 + \frac{1}{2}K_2\delta Q_2 + K_{12}\delta Q_1\delta Q_2 \quad (2)$$

where δQ_i is the charge imbalance on the i -th edge and K_i is the edge stiffness, while K_{12} is the coupling between the two edges. The case $K_{12} = 0$ corresponds to the scenario described in figure 2.

Assuming a small variation in the interfering diameter, we can calculate the charge using Eq. 1. We obtain $q_{\nu=2}/e = 1.98 \pm 0.18$ and $q_{\nu=4}/e = 2.55 \pm 0.35$, both of which are close to two electrons per period. Next, we calculate the flux oscillation period $\phi_{\nu=2}/\phi_0 = 1.78 \pm 0.56$ and $\phi_{\nu=4}/\phi_0 = 0.80 \pm 0.11$. These values can be interpreted as an average between two oscillation modes. We expect that for the two innermost interacting edges the flux period follows $\phi_{\nu_{int}}/\phi_0 = 1/(\nu_{int}(\nu_{int} - 1))$. This yields values of 1.5 for $\nu_{int} = 2$ and 0.58 for $\nu_{int} = 4$, which are in good agreement with our experimental results. This assumption is also in agreement with STM measurements of quantized energy levels in a graphene antidot, where phase slips have been observed due to the coupling of two antidot-bound states [34]. These slips are visible in figure 3-**c-d** in both $\nu = 2$ and $\nu = 4$ as diagonal jumps in the oscillations.

Finally, as we keep closing the constriction the inner edge is completely reflected and we get oscillations in the second edge as reported in the supplementary materials for $\nu = 2$.

CONCLUSION

Here we have demonstrated that a gate-defined bilayer graphene antidot is a versatile geometry for studying the inter-edge interaction in the quantum Hall regime, effectively avoiding bulk-to-edge interactions that typically are present in FPIs.

Our results reveal complete tunability over a range of variables and the ability to control inter-edge interactions. Notably, we find that Coulomb interactions between the propagating edge modes, often overlooked in similar studies, emerge as carrying the dominant energy scale, and their function is crucial for future studies in the fractional quantum hall regime.

Our findings highlight the significant role of bilayer graphene antidot as a platform for studying the quantum Hall effect and its potential for exploring quasiparticle interactions in the fractional quantum Hall regime.

-
- [1] B. I. Halperin, A. Stern, I. Neder, and B. Rosenow, Theory of the Fabry-Pérot quantum Hall interferometer, Phys. Rev. B **83**, 155440 (2011).
 [2] D. T. McClure, Y. Zhang, B. Rosenow, E. M. Levenson-

Falk, C. M. Marcus, L. N. Pfeiffer, and K. W. West, Edge-State Velocity and Coherence in a Quantum Hall Fabry-Pérot Interferometer, Phys. Rev. Lett. **103**, 206806 (2009).

- [3] N. Ofek, A. Bid, M. Heiblum, A. Stern, V. Umansky, and D. Mahalu, Role of interactions in an electronic Fabry–Perot interferometer operating in the quantum Hall effect regime, *Proc. Natl. Acad. Sci. U.S.A.* **107**, 5276 (2010).
- [4] C. Déprez, L. Veyrat, H. Vignaud, G. Nayak, K. Watanabe, T. Taniguchi, F. Gay, H. Sellier, and B. Saccépé, A tunable Fabry–Pérot quantum Hall interferometer in graphene, *Nat. Nanotechnol.* **16**, 555 (2021).
- [5] Y. Ronen, T. Werkmeister, D. Haie Najafabadi, A. T. Pierce, L. E. Anderson, Y. J. Shin, S. Y. Lee, Y. H. Lee, B. Johnson, K. Watanabe, T. Taniguchi, A. Yacoby, and P. Kim, Aharonov–Bohm effect in graphene-based Fabry–Pérot quantum Hall interferometers, *Nat. Nanotechnol.* **16**, 563 (2021).
- [6] H. Fu, K. Huang, K. Watanabe, T. Taniguchi, M. Kayyalha, and J. Zhu, Aharonov–Bohm Oscillations in Bilayer Graphene Quantum Hall Edge State Fabry–Pérot Interferometers, *Nano Lett.* **23**, 718 (2023).
- [7] J. Nakamura, S. Fallahi, H. Sahasrabudhe, R. Rahman, S. Liang, G. C. Gardner, and M. J. Manfra, Aharonov–Bohm interference of fractional quantum Hall edge modes, *Nat. Phys.* **15**, 563 (2019).
- [8] J. Nakamura, S. Liang, G. C. Gardner, and M. J. Manfra, Direct observation of anyonic braiding statistics, *Nat. Phys.* **16**, 931 (2020).
- [9] N. L. Samuelson, L. A. Cohen, W. Wang, S. Blanch, T. Taniguchi, K. Watanabe, M. P. Zaletel, and A. F. Young, Anyonic statistics and slow quasiparticle dynamics in a graphene fractional quantum Hall interferometer, [arXiv 10.48550/arXiv.2403.19628](https://arxiv.org/abs/10.48550/arXiv.2403.19628) (2024), 2403.19628.
- [10] T. Werkmeister, J. R. Ehrets, Y. Ronen, M. E. Wesson, D. Najafabadi, Z. Wei, K. Watanabe, T. Taniguchi, D. E. Feldman, B. I. Halperin, A. Yacoby, and P. Kim, Strongly coupled edge states in a graphene quantum Hall interferometer, *Nat. Commun.* **15**, 1 (2024).
- [11] J. Kim, H. Dev, R. Kumar, A. Ilin, A. Haug, V. Bhardwaj, C. Hong, K. Watanabe, T. Taniguchi, A. Stern, and Y. Ronen, Aharonov–Bohm interference and statistical phase-jump evolution in fractional quantum Hall states in bilayer graphene, *Nat. Nanotechnol.* , 1 (2024).
- [12] Y. Ji, Y. Chung, D. Sprinzak, M. Heiblum, D. Mahalu, and H. Shtrikman, An electronic Mach–Zehnder interferometer, *Nature* **422**, 415 (2003).
- [13] I. Neder, N. Ofek, Y. Chung, M. Heiblum, D. Mahalu, and V. Umansky, Interference between two indistinguishable electrons from independent sources, *Nature* **448**, 333 (2007).
- [14] H. K. Kundu, S. Biswas, N. Ofek, V. Umansky, and M. Heiblum, Anyonic interference and braiding phase in a Mach–Zehnder interferometer, *Nat. Phys.* **19**, 515 (2023).
- [15] V. Deviatov, S. V. Egorov, G. Biasiol, and L. Sorba, Quantum Hall Mach–Zehnder interferometer at fractional filling factors, *Europhysics Letters* **100**, 10.1209/0295-5075/100/67009 (2012).
- [16] B. Ghosh, M. Labendik, L. Musina, V. Umansky, M. Heiblum, and D. F. Mross, Anyonic Braiding in a Chiral Mach–Zehnder Interferometer, [arXiv 10.48550/arXiv.2410.16488](https://arxiv.org/abs/10.48550/arXiv.2410.16488) (2024), 2410.16488.
- [17] S. Levy Schreier, A. Stern, B. Rosenow, and B. I. Halperin, Reprint of : Thermodynamic properties of a quantum Hall anti-dot interferometer, *Physica E* **82**, 145 (2016).
- [18] H.-S. Sim, M. Kataoka, and C. J. B. Ford, Electron interactions in an antidot in the integer quantum Hall regime, *Phys. Rep.* **456**, 127 (2008).
- [19] S. Ihnatsenka, I. V. Zozoulenko, and G. Kirichenow, Electron-electron interactions in antidot-based Aharonov-Bohm interferometers, *Phys. Rev. B* **80**, 115303 (2009).
- [20] S. W. Hwang, J. A. Simmons, D. C. Tsui, and M. Shayegan, Quantum interference in two independently tunable parallel point contacts, *Phys. Rev. B* **44**, 13497 (1991).
- [21] C. J. B. Ford, P. J. Simpson, I. Zailer, D. R. Mace, M. Yosefin, M. Pepper, D. A. Ritchie, J. E. F. Frost, M. P. Grimshaw, and G. A. C. Jones, Charging and double-frequency Aharonov-Bohm effects in an open system, *Phys. Rev. B* **49**, 17456 (1994).
- [22] M. Kataoka, C. J. B. Ford, G. Faini, D. Maily, M. Y. Simmons, D. R. Mace, C.-T. Liang, and D. A. Ritchie, Detection of Coulomb Charging around an Antidot in the Quantum Hall Regime, *Phys. Rev. Lett.* **83**, 160 (1999).
- [23] H.-S. Sim, M. Kataoka, H. Yi, N. Y. Hwang, M.-S. Choi, and S.-R. E. Yang, Coulomb Blockade and Kondo Effect in a Quantum Hall Antidot, *Phys. Rev. Lett.* **91**, 266801 (2003).
- [24] V. J. Goldman and B. Su, Resonant Tunneling in the Quantum Hall Regime: Measurement of Fractional Charge, *Science* **267**, 1010 (1995).
- [25] V. J. Goldman, J. Liu, and A. Zaslavsky, Fractional statistics of Laughlin quasiparticles in quantum antidots, *Phys. Rev. B* **71**, 153303 (2005).
- [26] A. Kou, C. M. Marcus, L. N. Pfeiffer, and K. W. West, Coulomb Oscillations in Antidots in the Integer and Fractional Quantum Hall Regimes, *Phys. Rev. Lett.* **108**, 256803 (2012).
- [27] S. Das Sarma, M. Freedman, and C. Nayak, Topologically Protected Qubits from a Possible Non-Abelian Fractional Quantum Hall State, *Phys. Rev. Lett.* **94**, 166802 (2005).
- [28] C. Nayak, S. H. Simon, A. Stern, M. Freedman, and S. Das Sarma, Non-Abelian anyons and topological quantum computation, *Rev. Mod. Phys.* **80**, 1083 (2008).
- [29] S. H. Simon, Proposal for a quantum Hall pump, *Phys. Rev. B* **61**, R16327 (2000).
- [30] K. S. Novoselov, A. K. Geim, S. V. Morozov, D. Jiang, M. I. Katsnelson, I. V. Grigorieva, S. V. Dubonos, and A. A. Firsov, Two-dimensional gas of massless Dirac fermions in graphene, *Nature* **438**, 197 (2005).
- [31] Y. Zhang, Y.-W. Tan, H. L. Stormer, and P. Kim, Experimental observation of the quantum Hall effect and Berry’s phase in graphene, *Nature* **438**, 201 (2005).
- [32] S. Jung, G. M. Rutter, N. N. Klimov, D. B. Newell, I. Calizo, A. R. Hight-Walker, N. B. Zhitenev, and J. A. Stroscio, Evolution of microscopic localization in graphene in a magnetic field from scattering resonances to quantum dots, *Nat. Phys.* **7**, 245 (2011).
- [33] C. Gutiérrez, D. Walkup, F. Ghahari, C. Lewandowski, J. F. Rodriguez-Nieva, K. Watanabe, T. Taniguchi, L. S. Levitov, N. B. Zhitenev, and J. A. Stroscio, Interaction-driven quantum Hall wedding cake-like structures in graphene quantum dots, *Science* **361**, 789 (2018).
- [34] D. Walkup, F. Ghahari, C. Gutiérrez, K. Watanabe, T. Taniguchi, N. B. Zhitenev, and J. A. Stroscio, Tuning single-electron charging and interactions between compressible Landau level islands in graphene, *Phys. Rev. B* **101**, 035428 (2020).
- [35] S. M. Mills, A. Gura, K. Watanabe, T. Taniguchi,

- M. Dawber, D. V. Averin, and X. Du, Dirac fermion quantum Hall antidot in graphene, *Phys. Rev. B* **100**, 245130 (2019).
- [36] S. M. Mills, D. V. Averin, and X. Du, Localizing Fractional Quasiparticles on Graphene Quantum Hall Antidots, *Phys. Rev. Lett.* **125**, 227701 (2020).
- [37] B. M. Hunt, J. I. A. Li, A. A. Zibrov, L. Wang, T. Taniguchi, K. Watanabe, J. Hone, C. R. Dean, M. Zaitsev, R. C. Ashoori, and A. F. Young, Direct measurement of discrete valley and orbital quantum numbers in bilayer graphene, *Nat. Commun.* **8**, 1 (2017).
- [38] J. Li, Y. Tupikov, K. Watanabe, T. Taniguchi, and J. Zhu, Effective Landau Level Diagram of Bilayer Graphene, *Phys. Rev. Lett.* **120**, 047701 (2018).
- [39] V. J. Goldman, J. Liu, and A. Zaslavsky, Electron tunneling spectroscopy of a quantum antidot in the integer quantum Hall regime, *Phys. Rev. B* **77**, 115328 (2008).
- [40] T. Werkmeister, J. R. Ehrets, M. E. Wesson, D. H. Najafabadi, K. Watanabe, T. Taniguchi, B. I. Halperin, A. Yacoby, and P. Kim, Anyon braiding and telegraph noise in a graphene interferometer, *arXiv 10.48550/arXiv.2403.18983* (2024), 2403.18983.
- [41] J. Kim, H. Dev, R. Kumar, A. Ilin, A. Haug, V. Bhardwaj, C. Hong, K. Watanabe, T. Taniguchi, A. Stern, and Y. Ronen, Aharonov–Bohm interference and statistical phase-jump evolution in fractional quantum Hall states in bilayer graphene, *Nat. Nanotechnol.* **19**, 1619 (2024).
- [42] M. P. Rössli, L. Brem, B. Kratochwil, G. Nicolí, B. A. Braem, S. Hennel, P. Märki, M. Berl, C. Reichl, W. Wegscheider, K. Ensslin, T. Ihn, and B. Rosenow, Observation of quantum Hall interferometer phase jumps due to a change in the number of bulk quasiparticles, *Phys. Rev. B* **101**, 125302 (2020).
- [43] M. P. Rössli, M. Hug, G. Nicolí, P. Märki, C. Reichl, B. Rosenow, W. Wegscheider, K. Ensslin, and T. Ihn, Fractional Coulomb blockade for quasi-particle tunneling between edge channels, *Sci. Adv.* **7**, 10.1126/sciadv.abf5547 (2021).
- [44] W. Yang, D. Perconte, C. Déprez, K. Watanabe, T. Taniguchi, S. Dumont, E. Wagner, F. Gay, I. Safi, H. Sellier, and B. Sacépé, Evidence for correlated electron pairs and triplets in quantum Hall interferometers, *arXiv 10.48550/arXiv.2312.14767* (2023), 2312.14767.
- [45] Y. Barlas, R. Côté, K. Nomura, and A. H. MacDonald, Intra-Landau-Level Cyclotron Resonance in Bilayer Graphene, *Phys. Rev. Lett.* **101**, 097601 (2008).
- [46] J. Martin, B. E. Feldman, R. T. Weitz, M. T. Allen, and A. Yacoby, Local Compressibility Measurements of Correlated States in Suspended Bilayer Graphene, *Phys. Rev. Lett.* **105**, 256806 (2010).

METHODS

A. Sample fabrication

The device was fabricated using a standard van der Waals dry-transfer technique. First, graphene and hBN were mechanically exfoliated from bulk crystals on a SiO₂/Si substrate. The desired flakes are identified under optical microscope and atomic force microscopy to check for any flake impurity. The stack

was assembled using homemade poly(bisphenol A carbonate)/polydimethylsiloxane (PC/PDMS) to pick up all the flakes at a temperature ~ 90 °C. The stack was then transferred onto a doped silicon substrate with a 285 nm thick layer of thermally grown SiO₂ by melting the PC at a temperature of ~ 180 °C. The stack reported here has a 56 nm thick top hBN and a 33 nm thick bottom hBN layer.

Device patterning was achieved through multiple steps of electron beam lithography, followed by reactive ion etching and metal deposition. First, the TG contacts were created by depositing an 18 nm Pd layer. The device geometry was then defined through reactive ion etching, initially using O₂, followed by SF₆, and then another O₂ step. The electrode pattern was subsequently created by etching with SF₆ and O₂, followed by angled deposition of a 5/100 nm Cr/Au layer with rotation.

Finally, the TG was refined with 30-second O₂ etch steps. During each step, the two-probe resistance between each gate bridge-contact was monitored to ensure that all gates were fully separated while minimizing etching of the hBN and achieving narrow line widths [5].

B. Measurements

The device was measured in a BlueFors dry dilution refrigerator with a base temperature of ~ 10 mK. Electronic filters are installed on all transport lines to help thermalize electrons. Unless otherwise noted, a constant 5 T perpendicular magnetic field was applied. Resistance measurements are conducted using ZI lock-in amplifiers with a 1 V AC voltage excitation at a frequency of 33.333 Hz applied to a homemade voltage divider. A Yokogawa GS200 sets the DC bias. The current is measured through a current-to-voltage amplifier (K-tip variable gain transimpedance amplifier), and voltages are amplified at room temperature by 100 before being sent to the lock-in amplifier. For DC bias measurements, a homemade voltage adder is employed. Yokogawa GS200 is used to apply voltage to each gate. To improve the quality of the ohmic contacts, a positive voltage of $V_{Si} = 14.5$ V is applied to the silicon gate, doping the graphene layer next to the contacts in a highly electron-doped region. All measurements are performed in the electron-doped regime.

Author contributions

M.B., M.D.L. and Z.Z. conceived the project. M.B. supervised the project. M.D.L. fabricated the devices with inputs from Z.Z. and T.F. M.D.L. performed the measurements and analyzed the data with input from E.H. K.W. and T.T. provided the hBN crystals. M.D.L., E.H., F.K. and M.B. wrote the manuscript with input from all authors.

ACKNOWLEDGMENTS

The authors acknowledge M. Heiblum, T. Ihn and S. H. Simon for valuable discussions. M.D.L thanks M. Coraiola for the support in the COMSOL simulations. M.D.L, E.H and Z.Z acknowledge funding from SNSF. M.B. acknowledges the support of SNSF Eccellenza grant No. PCEGP2_194528, and support from the QuantERA II Programme that has received funding from the European Union's Horizon 2020 research and innovation program under Grant Agreement No 101017733. F.K. ac-

knowledges support from the European Research Council (ERC) as part of the project NONLOCAL under grant agreement No 856526. K.W. and T.T. acknowledge support from the JSPS KAKENHI (Grant Numbers 20H00354 and 23H02052) and World Premier International Research Center Initiative (WPI), MEXT, Japan.

Data availability

The data supporting the findings of this study are available from the corresponding author upon reasonable request.

SUPPLEMENTARY MATERIALS

Device Characterization

Figure S1 shows the optical microscope image of the device. From the measurements Hall conductance dependence, measured outside the antidot, we extract the BG capacitance per unit area $C_{bg} = 605 \pm 2 \mu\text{Fm}^{-2}$ and from the slope in figure S1-c the TG Capacitance $C_{tg} = 451 \pm 5 \mu\text{Fm}^{-2}$. Following the procedure in [41] the measured R_{xx} can be fitted with the following equation

$$R_{xx} = R_c + \frac{L/W}{\mu\sqrt{(C_{bg}(V_{bg} - V_{cnp}))^2 + (n_0e)^2}} \quad (3)$$

with R_c the contact resistance, L and W the length between two contacts and the width of the device respectively, μ the mobility and n_0 the intrinsic doping. From the best fit, shown in figure S1-b we find a mobility $\mu \simeq 180,000 \text{ cm}^{-2}\text{V/s}$ and a charge impurity of $n_0 = 1.1 \cdot 10^{10} \text{ cm}^{-2}$. We believe that the absence of fractional quantum Hall states at a field of $B = 8 \text{ T}$ is due to the relatively high density of charge impurities.

Figure S1-d presents finite element simulations of the electron density distribution in the device at zero magnetic field, conducted using COMSOL Multiphysics software. These simulations are based on a three-dimensional numerical solution of Poisson's equation and incorporate the screening effects of the electron gas within the Thomas-Fermi approximation. The model consists of two planar sheets where voltage is applied: the hBN layers as an insulator, and the bilayer graphene represented as a single-layer sheet. Inter-layer screening and band gap effects are artificially included in the model to account for their influence.

The simulations show a depletion of the antidot region as the BG voltage decreases, and an increase in the antidot area relative to its lithographically defined value. The antidot has a nominal diameter of 200 nm, but the electrostatic one is of $D = 290 \text{ nm}$. The results presented here correspond to gate voltages of $V_{bg} = -2 \text{ V}$, $V_{tg} = 0.8 \text{ V}$ and $V_{sg} = -2 \text{ V}$.

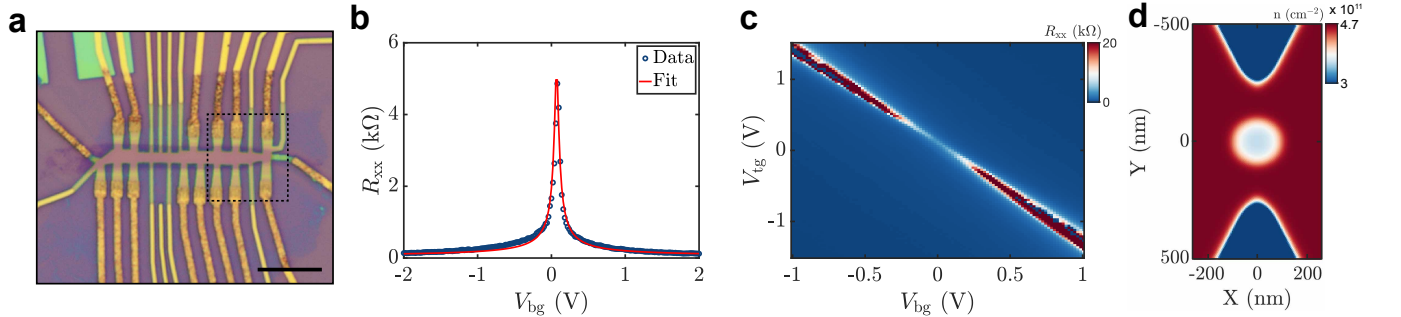


FIG. S1: Device Characterization **a**, Optical microscope image of the device. The scale bar is $10 \mu\text{m}$. **b**, Longitudinal resistance as a function of the BG in blue and best fit in red. **c**, Longitudinal resistance measured outside the antidot at $B = 0 \text{ T}$ as a function of the BG and TG voltage. **d**, COMSOL simulation of the studied geometry. The antidot has a nominal diameter of 200 nm, but the electrostatic one is of $D = 290 \text{ nm}$.

Oscillation in IQH

In this section, we report the analysis for the oscillations in all integer filling factors studied in the main text. Figure S2 shows the diagonal conductance G_d oscillations as a function of the BG voltage and magnetic field for filling factors $\nu = 1 - 4$ (a-d) and their 2D-FFT (e-h). For each plot, the inset schematically shows the interfering edge. Moreover, all oscillations display Coulomb diamond behavior as shown in panels i-n. The white arrow in panel i indicates the direction of increasing number of electrons bound to the antidot. From the diamonds, we can extract the energy required to add a new electron, the charging energy. It is highest at $\nu = 2$, followed by $\nu = 4$, $\nu = 1$, and finally $\nu = 3$. This trend aligns with the Landau level structure in bilayer graphene, where the Landau level gaps at $\nu = 4$, and $\nu = 2$, are the largest [46].

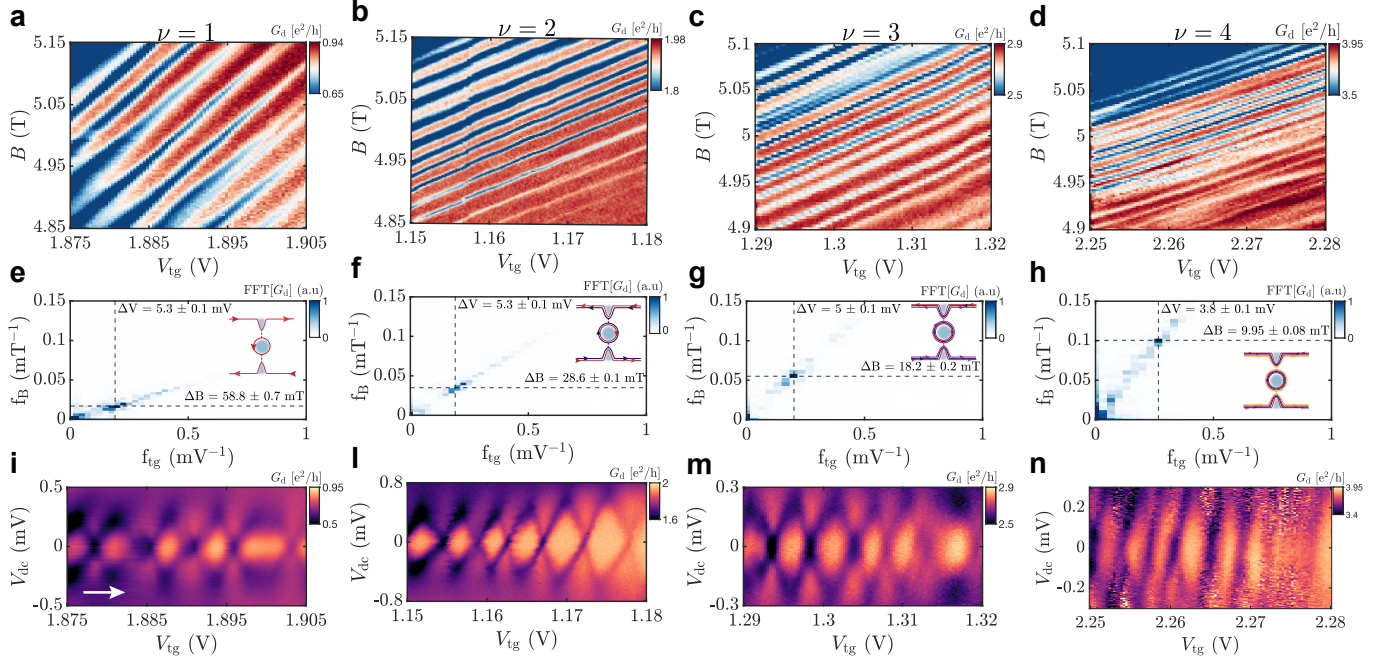


FIG. S2: Coulomb dominated oscillations. a-d, Diagonal conductance G_d oscillations as a function of the BG voltage and magnetic field for filling factors $\nu = 1 - 4$. e-h, 2D-FFT of the oscillations, the inset schematically shows the interfering edge. i-n, Diagonal conductance G_d oscillations as a function of BG voltage and dc bias, displaying the characteristic Coulomb diamonds. The white arrow in panel i indicates the antidot-bound electrons increasing direction. The Source-Drain measurements have been taken at $B = 5$ T.

Oscillation in Bottom Gate

As mentioned in the main text, another way to achieve oscillations is by varying the BG while keeping the TG constant. However, the drawback of this method is that the antidot potential and the side gates trenches are primarily controlled by the BG. Consequently, a small variation in the BG has a much larger effect on the potential landscape compared to a similar variation in the TG.

Figure S3a-c shows oscillations obtained in the BG at $\nu = 1 - 3$, with similar results to those observed in the TG. As shown in panels d-f, the magnetic field period closely matches the one obtained for TG oscillations, as reported in the main text and in figure S2. However, the BG period differs due to the thinner bottom hBN layer, which results in a larger capacitance.

Figure S3 panels l and m display the periods as a function of the filling factors. Complementary to the observations for TG oscillations, we find that the computed charge is 5% smaller than the expected value of one electron per cycle. This discrepancy arises from a shift in the antidot energy levels while varying the BG. While increasing the TG voltage expands the antidot area, causing the antidot energy levels to shift upward along the antidot potential and thereby increasing the measured gate oscillation period, the opposite occurs for the BG. As the BG voltage increases, the antidot area shrinks, leading to a downward shift in the energy levels, which in turn decreases the measured gate oscillation period.

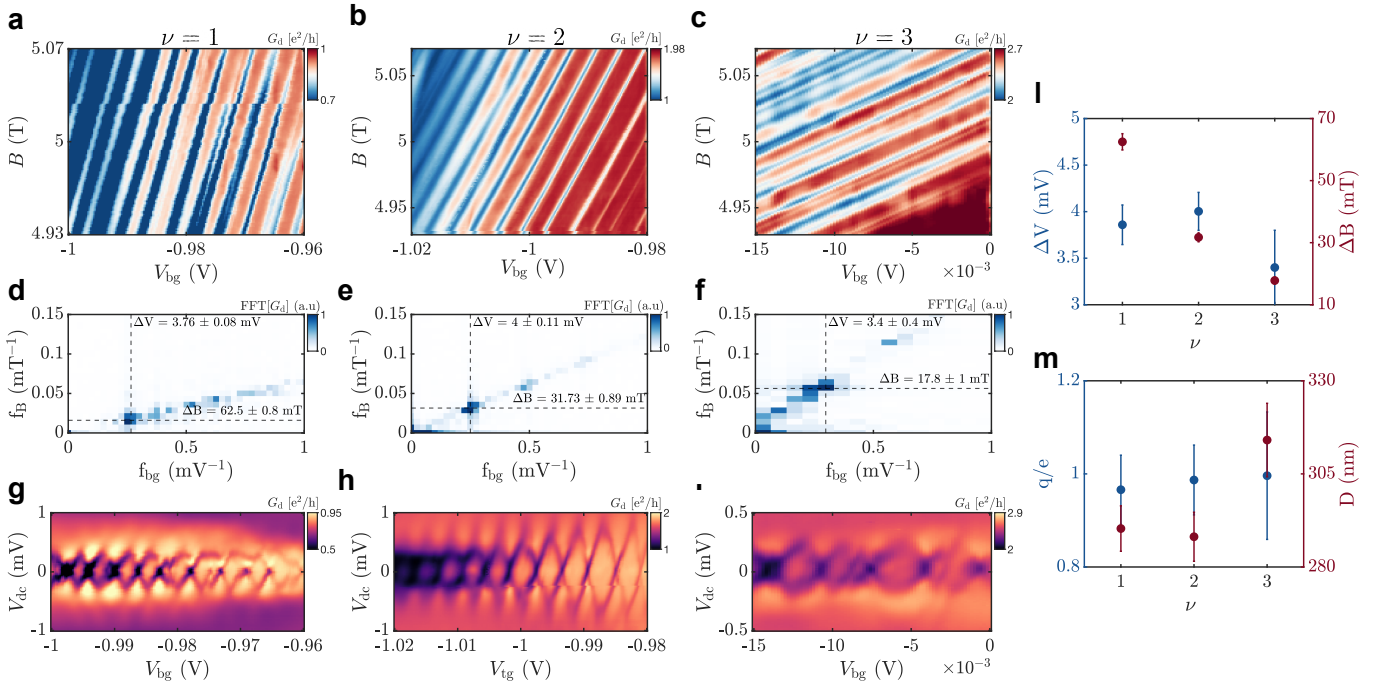


FIG. S3: Oscillations in bottom gate. a-c, Diagonal conductance G_d oscillations as a function of the bottom gate voltage and magnetic field for filling factors $\nu = 1 - 3$. d-f, 2D-FFT of the oscillations. g-i, Diagonal conductance G_d oscillations as a function of bottom gate voltage and DC bias, displaying the characteristic Coulomb Diamonds. The white arrow in panel i indicates the antidot-bound electrons increasing direction. The Source-Drain measurements have been taken at $B = 5$ T. l, Bottom Gate period ΔV (blue) and magnetic Field period ΔB (red) in function of the filling factor ν . m, Tunneling charge (blue) and oscillating antidot diameter (red) in function of the filling factor ν .

Oscillation in Area

Another way to induce gate oscillations is by modifying the antidot potential, which in turn changes the antidot area. This can be achieved by sweeping both the TG and the BG simultaneously while maintaining a constant bulk filling factor. As the antidot potential increases, so does its area, and to preserve a constant flux, the bound edge states shift to higher energy. An oscillation occurs when the chemical potential of an antidot-bound state aligns with the source chemical potential, as schematically illustrated in S4-a.

The equation for constant density lines is given by

$$V_{\text{tg}} = -1.34V_{\text{bg}} + \beta \quad (4)$$

where $\beta = \frac{e^2\nu B}{hC_{\text{tg}}}$ defines the filling factor.

Figure S4-b-c illustrates the area oscillations in both regimes of $\nu = 2$. The oscillations exhibit an opposite slope compared to density oscillations due to the opposite direction in which the energy levels move with respect to the increasing direction of the area, as indicated by the white arrow in figure S4-b.

The 2D-FFT analysis in figure S4-d reveals a magnetic field period comparable to that observed in density oscillations, while the gate voltage period appears larger.

In the *strongly coupled* regime (Figure S4c,e), the area-induced oscillation period is approximately 1.2 times larger than that in the *weakly coupled* regime. This value differs from the one observed for density oscillations in the main text, where the period increase is close to 2. We attribute this discrepancy to the different capacitive coupling of the antidot-bound states to the antidot potential (controlled simultaneously by both the TG and BG), which differs for different edges

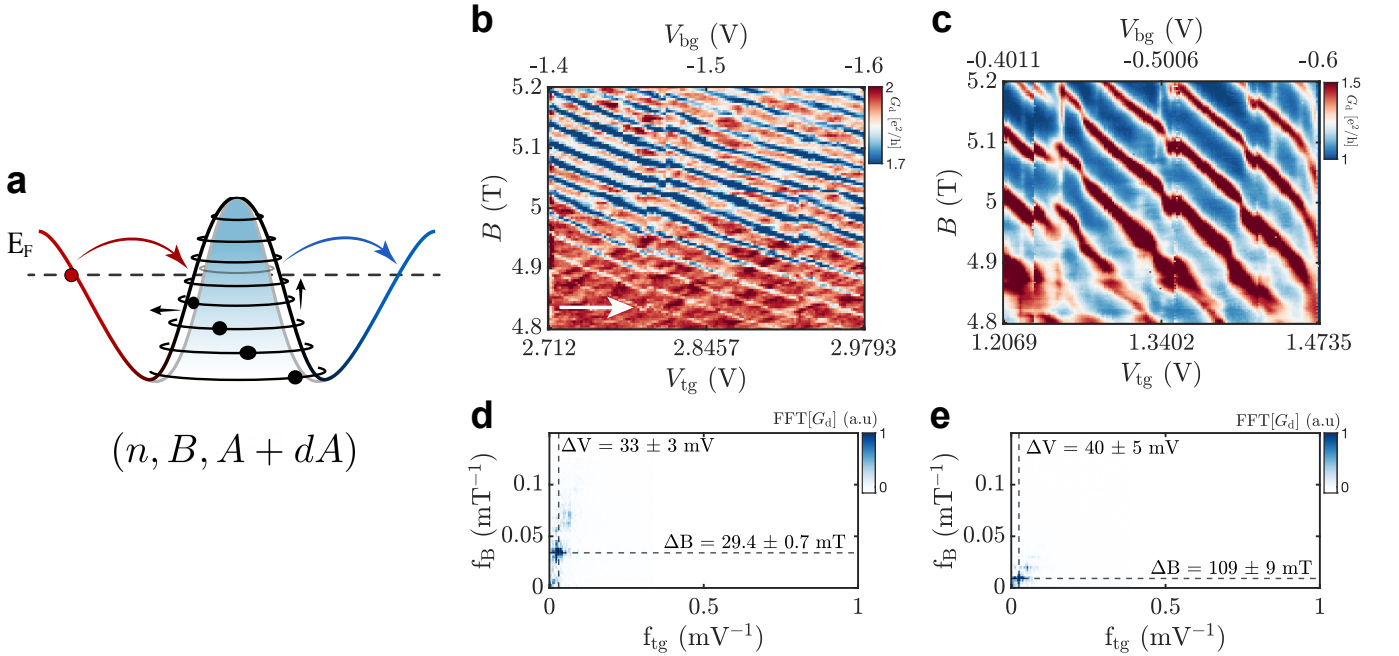


FIG. S4: Oscillations in the antidot area. **a** Schematic of the tunneling when changing the antidot area. **b-c**, Diagonal conductance G_d oscillations as a function of the bottom gate voltage and magnetic field for filling factor $\nu = 2$ in the weakly and strongly coupled regimes, respectively. **d-e**, 2D-FFT of the oscillations.

Outer Edge in $\nu = 2$

As the constriction filling factor continues to decrease, the inner edge can become completely reflected, allowing the outer edge to start interfering. In this case, we expect the magnetic field oscillation period to be ϕ_0/ν_{int} with $\nu_{\text{int}} = \nu_b - 1$.

Figure S5-a shows oscillations for the outer edge at a filling factor of 2 ($\nu_b = 2$, $\nu_{\text{int}} = 1$). From the 2D-FFT, we extract a magnetic field period of $\Delta B = 73 \pm 10$ mT, which is similar to that of the inner edge at filling factor 1. This corresponds to a flux period of ϕ_0 and an antidot diameter of $D = 269 \pm 18$ nm. Since the oscillations are gate-induced, we cannot directly extract the interfering charge.

Source-drain measurements, shown in figure S5-c, still display a Coulomb-dominated pattern with a charge excitation energy of $E = 210 \pm 10$ μeV .

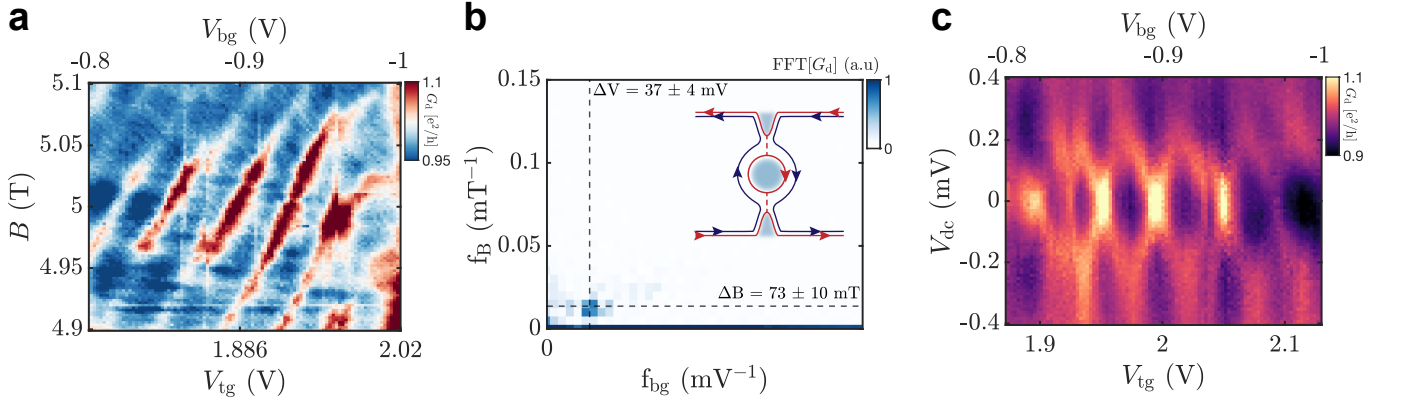


FIG. S5: Oscillations in the outer edge of $\nu = 2$ **a** Diagonal conductance G_d oscillations as a function of the antidot area magnetic field for the outer edge of filling factor $\nu = 2$. **b**, 2D-FFT of the oscillations. The insert schematically shows the outer edge interfering while the inner one is fully reflected. **c**, Diagonal conductance G_d oscillations as a function of the antidot area DC bias.

Theoretical Model for the strongly coupled regime

The pairing between two bound edge-states can be understood using a capacitive coupling model similar to the one used to describe bulk-edge coupling in a FPI [1]. We model the antidot as at $\nu = 0$, encircled by only two edge modes denoted 1 and 2 (inner and outer respectively). The filling factor between the two edges mode is ν_1 and the constriction filling factor is ν_2 .

Assuming no tunneling between the edges, the total energy of the system can be written as

$$E = \frac{1}{2}K_1\delta Q_1 + \frac{1}{2}K_2\delta Q_2 + K_{12}\delta Q_1\delta Q_2 \quad (5)$$

where K_i is the edge stiffness, while K_{12} is the coupling between the two edges. For the states to be stable they must satisfy $K_1K_2 > K_{12}^2$

δQ_i is the charge imbalance on the two edges and can be expressed as

$$\begin{aligned} \delta Q_1 &= N_1e + \frac{A\delta B\Delta\nu_1}{\phi_0} - \delta VC_1A \\ \delta Q_2 &= (N_2 - N_1)e + \frac{A\delta B\Delta\nu_2}{\phi_0} + \delta VC_2A \end{aligned} \quad (6)$$

with C_i is the capacitive coupling of the TG to the i -th edge. The terms $\Delta\nu_i$ are related to the quantized Hall conductance on different incompressible regions and can be written as $\Delta\nu_1 = \nu_1$ and $\Delta\nu_2 = \nu_2 - \nu_1$.

By minimizing the energy in Eq. 2 as a function of δQ_1 we get the modified periods

$$\Delta B^s = \frac{\Delta B}{1 - \frac{K_{12}}{K_1}\left(\frac{\nu_1}{\nu_2}\right)} \quad (7)$$

$$\Delta V_{\text{tg}}^s = \frac{C_{\text{tg}}\Delta V_{\text{tg}}}{C_2 - C_1\frac{K_{12}}{K_1}} \quad (8)$$

As expected, the period of two coupled edges in the antidot is always larger than the uncoupled one, in opposition to what happens in a Fabry-Perot interferometer [40]. Moreover, we notice that the increase in gate period does not depend on the filling factor but only on the coupling between the edges. Using $\nu_2 = \nu_1 - \nu_2$ we get the values extracted from the 2D-FFT we get $\frac{K_{12}}{K_1}|_{\nu=2} = 0.72 \pm 0.03$ and $\frac{K_{12}}{K_1}|_{\nu=4} = 0.54 \pm 0.05$.

For the density variation using one of the gates, the calculation is more complicated, because we expect the TG to be capacitively coupled much more to the first edge, relative to the second edge, so we have not further developed the computations.

Oscillations in the strongly coupled regime at $\nu = 2$

We report here supplementary oscillations of the strongly coupled regime for $\nu = 2$ at $B = 5$ T. Figure S8-**a** shows a large scan that goes from the *weakly coupled* regime marked by the red dot characterized by $\phi_0/2$ and e oscillations, to the *strongly coupled*, marked by the yellow star, characterized by $3\phi_0/2$ and $2e$ oscillations. The transition between the two regimes is continuous and in the middle region shown in figure S8-**b** (for a different back gate voltage), it is possible to observe the superposition of the two oscillations modes as observed by [40, 44]. Finally S8-**c-d** show the oscillations in the *strongly coupled* regime for different back gate values.

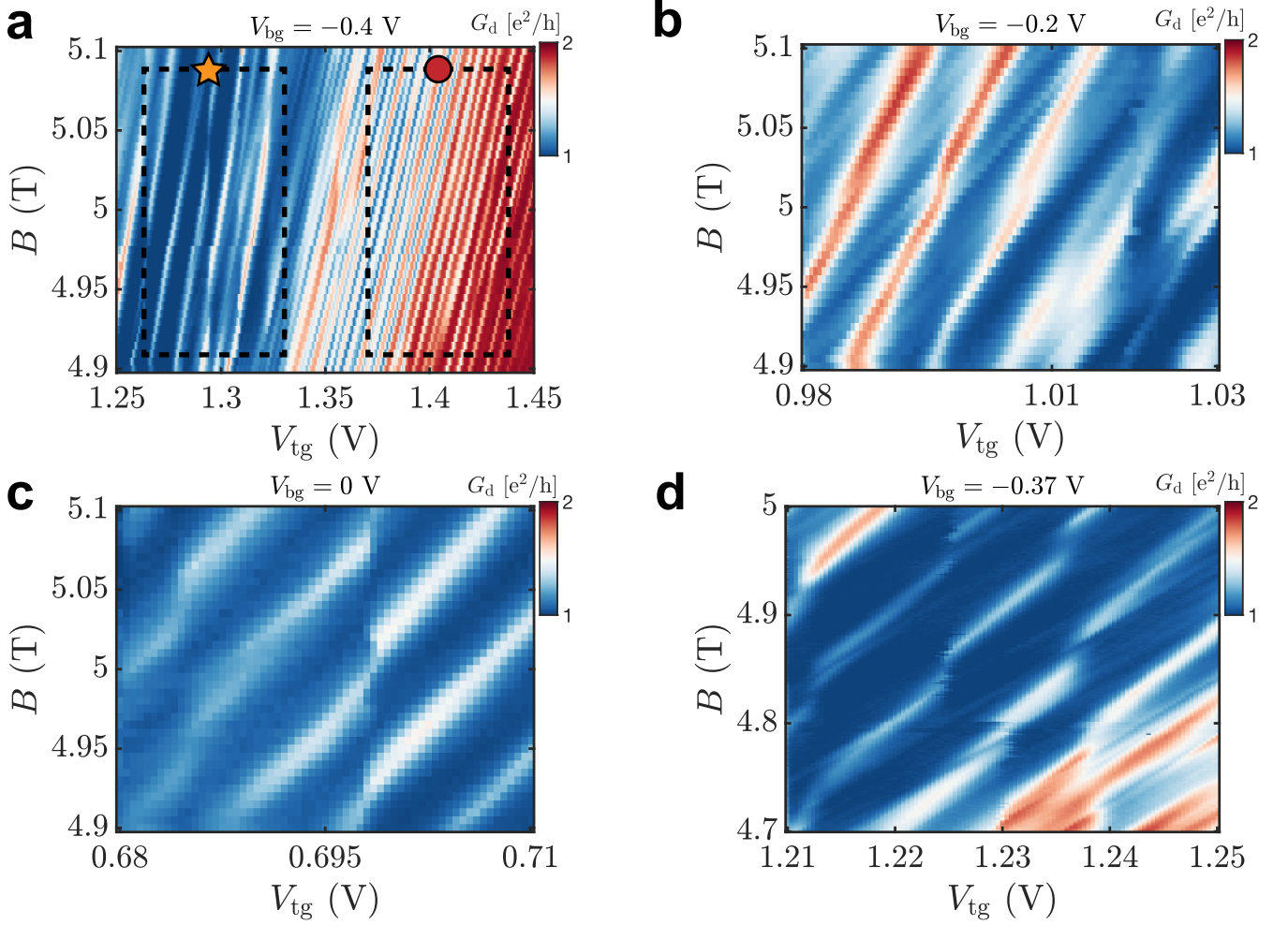


FIG. S8: Supplementary oscillations at $\nu = 2$ in the strongly coupled regime **a**, Diagonal conductance oscillations at $B = 5$ T in function of the top gate and the magnetic field over a large gate range. The oscillations continuously transition from the *weakly coupled* regime marked by the red dot to the *strongly coupled*, marked by the yellow star. **b**, Diagonal conductance oscillations in a gate voltage where both kinds of oscillation are visible. **c-d**, Diagonal conductance oscillations in the *strongly coupled* regime for two different back gate values.

Oscillations in the strongly coupled regime at $\nu = 4$

We report here supplementary oscillations from the weakly coupled to the strongly coupled regime for $\nu = 4$ at $B = 5$ T. The oscillations in figure S9b-c exhibit a larger period, as explained in the main text.

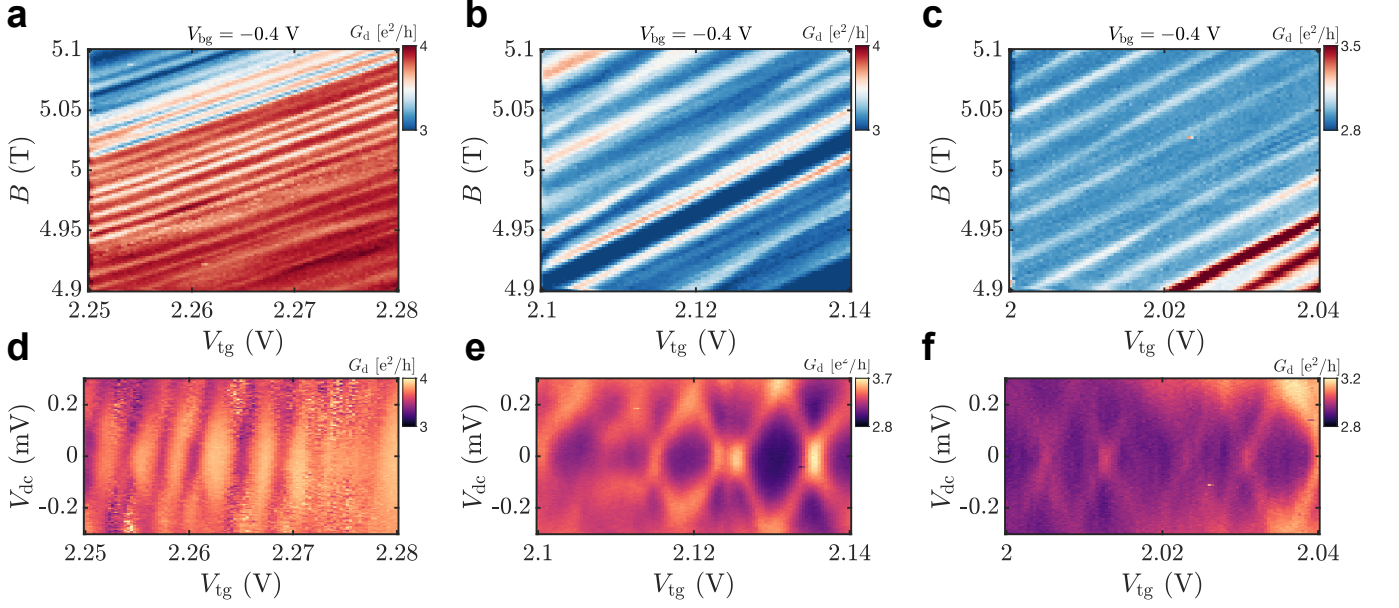


FIG. S9: Supplementary oscillations at $\nu = 4$ a-c, Diagonal conductance oscillations at $\nu = 4$ at $B = 5$ T in function of the top gate and the magnetic field at different back gate voltages.

Gate Voltages used for figures in the main text

In Table I we report the gate voltages corresponding to figures in the main text. When the voltage was the sweeping one it is not indicated.

Figure	V_{bg} (V)	V_{tg} (V)
Fig. 1- a	/	0
Fig. 1- b	0	0.725
Fig. 2- a	-0.2	/
Fig. 2- b	0	/
Fig. 2- c	-0.2	/
Fig. 2- d	-0.4	/
Fig. 3- a $\nu = 4$	0	/
Fig. 3- a $\nu = 3$	-0.1	/
Fig. 3- a $\nu = 2$	-0.6	/
Fig. 3- a $\nu = 1$	1	/
Fig. 3- c	-0.6	/
Fig. 3- d	0	/

TABLE I: Fixed voltages for main figures